Journal of Advanced Research 38 (2022) 143–155

Contents lists available at ScienceDirect

Journal of Advanced Research

journal homepage: www.elsevier.com/locate/jare

Pre-oxidation induced *in situ* interface strengthening in biodegradable Zn/nano-SiC composites prepared by selective laser melting

Chengde Gao [a], Meng Yao [a], Shuping Peng [b,c], Wei Tan [d,e,*], Cijun Shuai [a,f,*]

[a] State Key Laboratory of High Performance Complex Manufacturing, College of Mechanical and Electrical Engineering, Central South University, Changsha 410083, China
[b] NHC Key Laboratory of Carcinogenesis, The Key Laboratory of Carcinogenesis and Cancer Invasion of the Chinese Ministry of Education, School of Basic Medical Science, Central South University, Changsha 410078, China
[c] School of Energy and Machinery Engineering, Jiangxi University of Science and Technology, Nanchang 330013, China
[d] Department of Spine Surgery, The Third Xiangya Hospital of Central South University, Changsha 410013, China
[e] Department of Spinal Orthopedics, Huizhou Third People's Hospital, Guangzhou Medical University, Huizhou 516002, China
[f] Institute of Bioadditive Manufacturing, Jiangxi University of Science and Technology, Nanchang 330013, China

HIGHLIGHTS

- Zn/nano-SiC biocomposites were prepared *via* pre-oxidation and selective laser melting.
- In situ reaction improved the interface bonding between nano-SiC and the Zn matrix.
- The improved interfacial bonding enhanced the mechanical properties of the biocomposite.
- The biocomposite exhibited favorable biocompatibility on cell proliferation and adhesion.

GRAPHICAL ABSTRACT

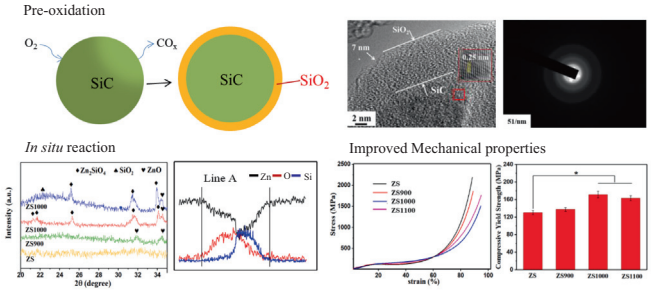

ARTICLE INFO

Article history:
Received 21 February 2021
Revised 16 August 2021
Accepted 30 September 2021
Available online 5 October 2021

Keywords:
Pre-oxidation
Interfacial strengthening
Zn/nano-SiC biocomposites
In situ reaction
Selective laser melting

ABSTRACT

Introduction: Nano-SiC has attracted great attention as ceramic reinforcement in metal matrix composites, but the weak interface bonding between them remains a bottleneck for efficient strengthening.
Objective: In this study, pre-oxidation treatments and selective laser melting (SLM) were employed to prepare Zn/nano-SiC biocomposites with strengthened interface bonding *via in situ* reaction.
Methods: Nano-SiC and Zn powders were pre-oxidized respectively, and then used to prepare Zn/nano-SiC biocomposites *via* SLM. The powder microstructure, and the interface characteristics and mechanical properties of the biocomposites were investigated. The degradation properties and cell response were analyzed to evaluate their feasibility for orthopedic applications.
Results: The results indicated that the pre-oxidation treatments generated a uniform oxide layer on the surface of both nano-SiC and Zn particles and the thickness of the oxide layer increased with pre-oxidation temperature. During the SLM process, the oxide layers not only improved the metal-ceramic wettability by reducing interface energy, but also induced *in situ* reaction to form chemical bonding between the Zn matrix and nano-SiC, thereby improving the interface bonding. Consequently, the Zn biocomposite reinforced by nano-SiC with a pre-oxidation temperature of 1000 °C (ZS1000 biocomposite) exhibited more transgranular fracture and significantly enhanced compressive yield strength of 171.5 MPa, which was 31.6% higher than that of the Zn biocomposite reinforced by nano-SiC without

Peer review under responsibility of Cairo University.

* Corresponding authors at: Department of Spine Surgery, The Third Xiangya Hospital of Central South University, Changsha 410013, China (W. Tan). State Key Laboratory of High Performance Complex Manufacturing, College of Mechanical and Electrical Engineering, Central South University, Changsha 410083, China (C. Shuai).

E-mail addresses: tanwei819@csu.edu.cn (W. Tan), shuai@csu.edu.cn (C. Shuai).

https://doi.org/10.1016/j.jare.2021.09.014

pre-oxidation. Moreover, the ZS1000 biocomposite presented slightly accelerated degradation which might be ascribed to the facilitated electron transfer by the interface product (Zn_2SiO_4). In addition, the ZS1000 biocomposite also showed appropriate biocompatibility for MG-63 cell adhesion, growth, and proliferation.

Conclusion: This study shows the potential practical applicability for the preparation of Zn-based biocomposites with strong interface bonding and mechanical properties for orthopedic applications.

Introduction

Zn, as a promising biodegradable metal, has received significant attention for implant applications due to its appropriate degradability and osteogenesis properties [1–3], but is limited by the inadequate mechanical strength [4]. Metal matrix composites (MMCs) have been proposed as a feasible approach to optimize the properties of metals. Among various reinforcements, SiC possesses outstanding mechanical performance and is also known as a kind of bioceramics with good biocompatibility and positive effect on osteoblasts [5–7]. Thus, it can be a potential candidate to improve the mechanical properties of Zn. Unfortunately, due to the great differences in physicochemical properties, SiC and metal matrix usually present poor wettability and weak interface bonding, which play a curial role in the final mechanical performance of MMCs [8]. Therefore, strong interfacial bonding remains a major challenge in SiC reinforced Zn-based MMCs.

Until now, many methods have been explored to improve the interface bonding in SiC reinforced MMCs, including surface metallization [9–11], matrix alloying [12,13], etc. Park et al. [14] introduced a Ni coating on SiC to ameliorate the interfacial characteristics in SiC reinforced Al-Zn alloys. The result showed that the Ni coating decreased the interfacial energy between SiC and the metal matrix, and led to a 51.2% enhancement of the interface bonding strength in the alloys. Hashim et al. [15] reported that alloying elements (such as Mg, Zr, etc.) could improve the wettability between SiC and metal matrix by reducing the surface tension of molten metal, which was in favor of the interface bonding in SiC reinforced MMCs. However, Panthglin et al. [13] and Gul et al. [16] revealed that the alloying of Mg in Al-SiC MMCs also easily led to the formation of pores and the reduced fluidity of Al matrix due to the low melting point constituents, which deteriorated the mechanical properties of the MMCs. These methods are difficult to control the influence of metal additions on the resulting properties of MMCs, or even cause bio-safety issues. It is necessary to find a practical method to enhance the interfacial bonding of Zn-based MMCs for biodegradable implant applications.

In situ interfacial reaction was also an effective approach to improve the interface bonding in MMCs [17–19]. Wang et al. [20] synthesized GO/ZnO to reinforce Mg-Zn alloy and found that ZnO could react with the metal matrix and improve the interface wetting, and the formation of a MgO interface layer enhanced the interface bonding between the reinforcement and metal matrix. Li et al. [21] introduced *in situ* reaction in Cu-Al_2O_3 MMCs through a CuO coating, and a continuous $CuAlO_2$ interface layer was formed between the Al_2O_3 reinforcement and Cu matrix, which significantly enhanced the interface bonding and further the bending strength of the MMCs. Therefore, *in situ* interface reaction might be a promising method to improve the interface bonding in Zn-SiC MMCs. Nevertheless, previous studies have shown that interface reaction can hardly occur between SiC and Zn [22], which limits the feasibility of *in situ* interface strengthening in Zn-SiC MMCs. Consequently, there have been few reports on the improvement of interface bonding of Zn-SiC MMCs, especially in the field of bone implant applications.

Recently, *in situ* reaction was reported between ZnO and SiO_2 by the diffusion of Zn^{2+} and O^{2-} into the SiO_2 shell [23]. As we know, the main advantages of *in situ reaction* includes not only improved wetting between metal melt and the reinforcing phase during the preparing process, but also the formation of chemical bonding at the interface of metal matrix and the reinforcing phase. Moreover, SiO_2 has been proven to promote the interfacial wetting between SiC and metals [24,25]. The novelty of this study lies in the introduction of *in situ* interface reaction in Zn-SiC MMCs by a combined process of pre-oxidation and selective laser melting (SLM). And the main objectives of this study were to improve the interfacial wettability and induce *in situ* reaction, thereby enhancing the interface bonding and further the mechanical properties of Zn-SiC MMCs. Concretely, nano-SiC and Zn powders were treated by pre-oxidation to form surface oxide layers, respectively, and then used to prepare Zn/nano-SiC biocomposites *via* SLM. During the SLM process, the oxide layers were expected to improve the interfacial wettability and induce *in situ* reaction between nano-SiC and Zn. The effects of pre-oxidation temperature on the powder microstructure, and the resulting interface characteristics and mechanical properties of the biocomposites were investigated in detail. Additionally, the degradability and biocompatibility of the biocomposites were also studied to evaluate their practicability for implant applications.

Experiments

Pre-oxidation treatments

Commercial Zn (≥99.9 wt% purity, ~60 μm) and nano-SiC particles (≥99.9 wt% purity, ~50 nm) were purchased from Shanghai Naiou Nanotechnology Co. Ltd. (China). The nano-SiC particles were first pre-oxidized in a tube furnace (GS1200-100, Yagelong Co. Ltd., China) at 900 °C, 1000 °C, and 1100 °C, respectively, with a holding time of 2 h (Fig. 1). And the Zn particles were also pre-oxidized in the tube furnace at 200 °C for 2 h. Subsequently, the nano-SiC particles with and without pre-oxidation treatments were ultrasonic dispersed respectively, and the pre-oxidized Zn particles were separately dispersed under magnetic stirring. The above nano-SiC solutions were then added into the Zn solution with continuous magnetic stirring to obtain mixture solutions containing nano-SiC with or without pre-oxidation treatments. Next, the mixture solutions were wet milled in absolute ethyl alcohol at 100 r/min for 2 h. Finally, the mixture solutions were filtered, and then dried to acquire the mixed powders with or without pre-oxidation treatments (weight ratio of Zn/nano-SiC was 2:98) for preparing biocomposites.

SLM preparation

A self-assembled SLM system, mainly consisting of a fiber laser, a scanning galvanometer, a computer-control system and gas cycle

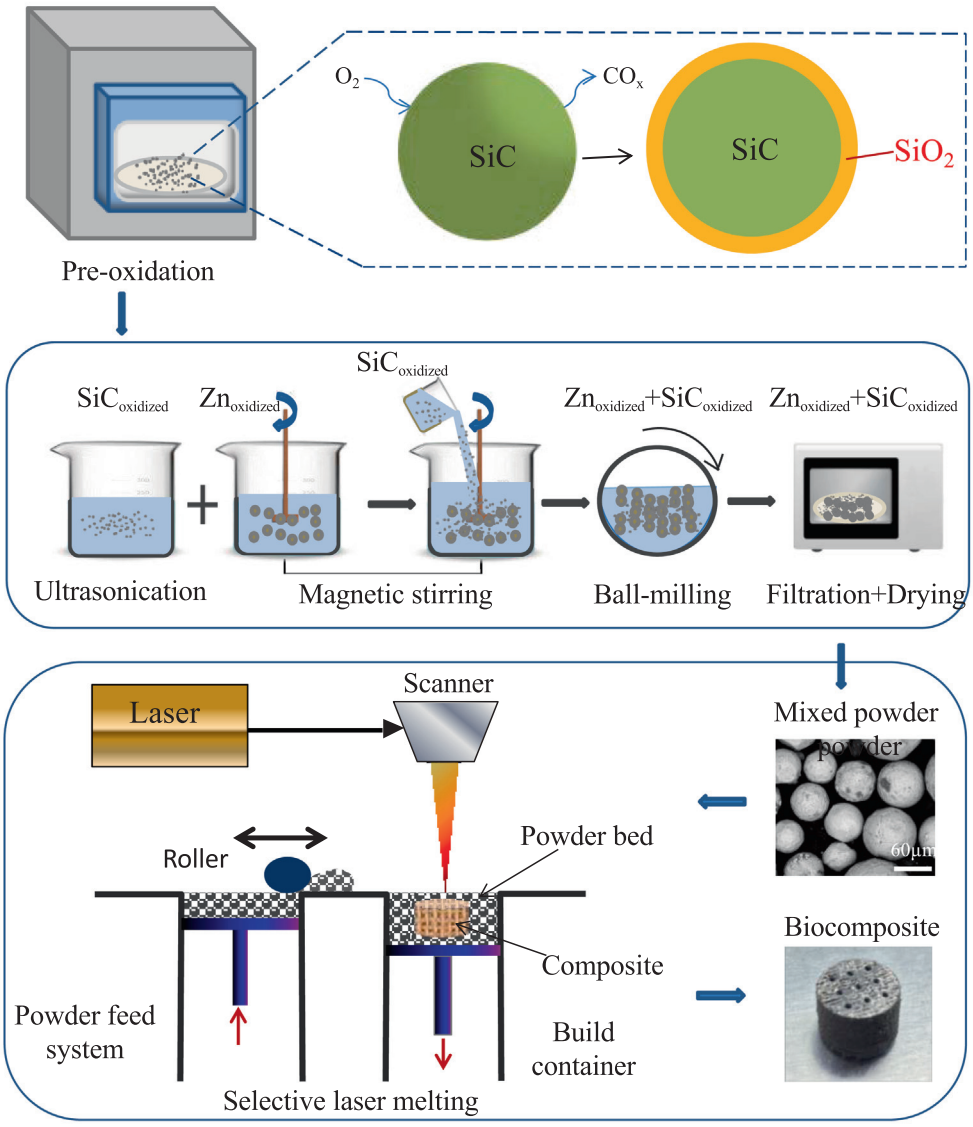

Fig. 1. A flow diagram for the preparation of pre-oxidized Zn/nano-SiC mixed powder and Zn/nano-SiC biocomposites. ($Zn_{oxidized}$ and $SiC_{oxidized}$ represent the pre-oxidized Zn and nano-SiC particles, respectively.)

equipment, was employed to fabricate Zn/nano-SiC biocomposites. In this study, a series of preliminary experiments were conducted to prepare Zn/nano-SiC biocomposites and a set of optimum processing parameters was obtained with laser power 85 W, scanning rate 150 mm/s, spot diameter 50 μm, scanning spacing 80 μm and layer thickness 0.1 mm. For brevity, the biocomposites containing nano-SiC without and with pre-oxidation treatments at 900 °C, 1000 °C and 1100 °C were designated as ZS, ZS900, ZS1000 and ZS1100 biocomposites, respectively.

Microstructure

X-ray diffractometer (XRD, D8 Advance, Bruker AXS, Germany) and X-ray photoelectron spectroscopy (XPS, ESCALAB 250Xi, Thermo Fisher Scientific, USA) tests were employed to identify the phase composition and analyze the chemical bonds on the surface of nano-SiC particles, respectively. For particle morphology and oxide layer analysis, the nano-SiC particles with and without pre-oxidation treatments were separately ultrasonic dispersed, and then dripped on copper foils and observed *via* transmission electron microscopy (TEM, Tecnai G2 F20, FEI, USA). The sizes of the nano-SiC particles were collected by image software from the TEM micrographs for statistical analysis. Moreover, a fast fourier transform (FFT) was conducted on the high-resolution TEM (HRTEM) micrographs by using digital micrograph software to evaluate the thickness of the oxide layers.

The average sizes of the Zn particles with and without pre-oxidation treatments were measured by a Marvin laser particle size meter (Mastersizer 3000, Malvern Instruments Co. Ltd., UK). The Zn particles and Zn/nano-SiC biocomposites were inlaid in hot inlay, polished, and then characterized by scanning electron microscopy (SEM, Phenom ProX, Phenom-World BV, Netherlands) equipped with energy disperse spectroscopy (EDS, INCA, Oxford Instruments, UK). The grain sizes of the biocomposites were also collected through image software and represented by mean values ± standard deviations. The phase compositions of the

biocomposites were determined by the above-mentioned XRD from 0 ~ 90° at 2°/min. And the fracture surfaces of the biocomposites were observed by SEM to evaluate the fracture modes.

Mechanical performance

The compressive strength of the Zn/nano-SiC biocomposites was measured using a universal testing machine (ZLC-50M, Jinan Zhongluchang Instruments Co. Ltd., China) at a loading rate of 0.2 mm/min under room temperature. All compression test samples were prepared as cylinder (Φ 3 × 6 mm) according to ASTM E9-89 standard [26]. At least three samples were measured for every group to obtain the corresponding stress and strain values. The microhardness of the biocomposites was examined *via* a Vickers hardness testing device (HXD-1000TM/LCD, Shanghai Taiming Optiacal Instrument Co. Ltd., China) at a loading force of 2.94 N for 15 s. At least 15 measurements were taken equidistantly on each sample for statistical analysis.

Electrochemical characteristics

The electrochemical measurements were conducted in simulated body fluid (SBF, 8.036 g/L NaCl, 0.354 g/L $NaHCO_3$, 0.311 g/L $MgCl_2{\cdot}6H_2O$, 0.292 g/L $CaCl_2$, 0.231 g/L $K_2HPO_4{\cdot}3H_2O$ and 0.225 g/L KCl, pH 7.4 [27]) solutions at an electrochemical workstation (Autolab M204, Metrohm, Switzerland). A three-electrode system was adopted for electrochemical tests with a saturated calomel electrode as the reference electrode, a platinum counter electrode as the counter electrode, and the biocomposites as the working-electrode. Firstly, the samples were dipped into SBF for 3600 s until the open circuit potential (OCP) reached a steady state. Electrochemical impedance spectroscopy (EIS) analysis was carried out over frequencies ranging from 10^5 Hz to 10^{-2} Hz with 10 mV perturbation. Next, potentiodynamic polarization measurements were conducted from −0.5 V to −1.7 V (vs. OCP) at a speed of 1 mV/s. Finally, the corrosion potential (E_{corr}) and corrosion current density (i_{corr}) were obtained by using linear extrapolation on the basis of the Tafel method, and the relevant corrosion rates were computed based on ASTM-G102-89 standard [28].

Degradation behavior

In vitro degradation behavior of the biocomposites was evaluated by immersion method. All samples were polished and cleaned by ultrasonic. Subsequently, each sample was soaked in an airtight container with SBF solution based on ASTM G31-72 standard (sur-

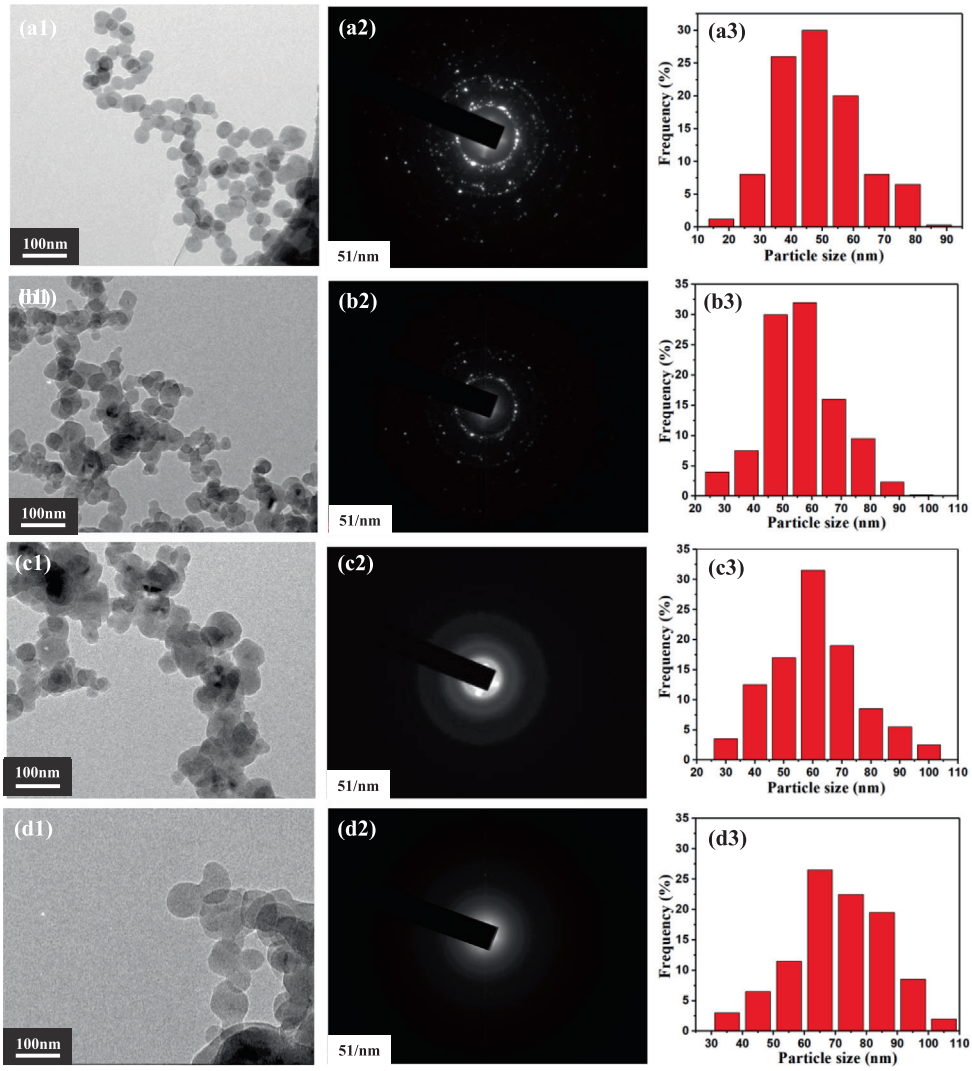

Fig. 2. Bright-field TEM micrographs of (a1) nano-SiC particles and pre-oxidized nano-SiC particles at (b1) 900 °C, (c1) 1000 °C, and (d1) 1100 °C, and corresponding (a2-d2) SAED micrographs and (a3-d3) particles size distribution.

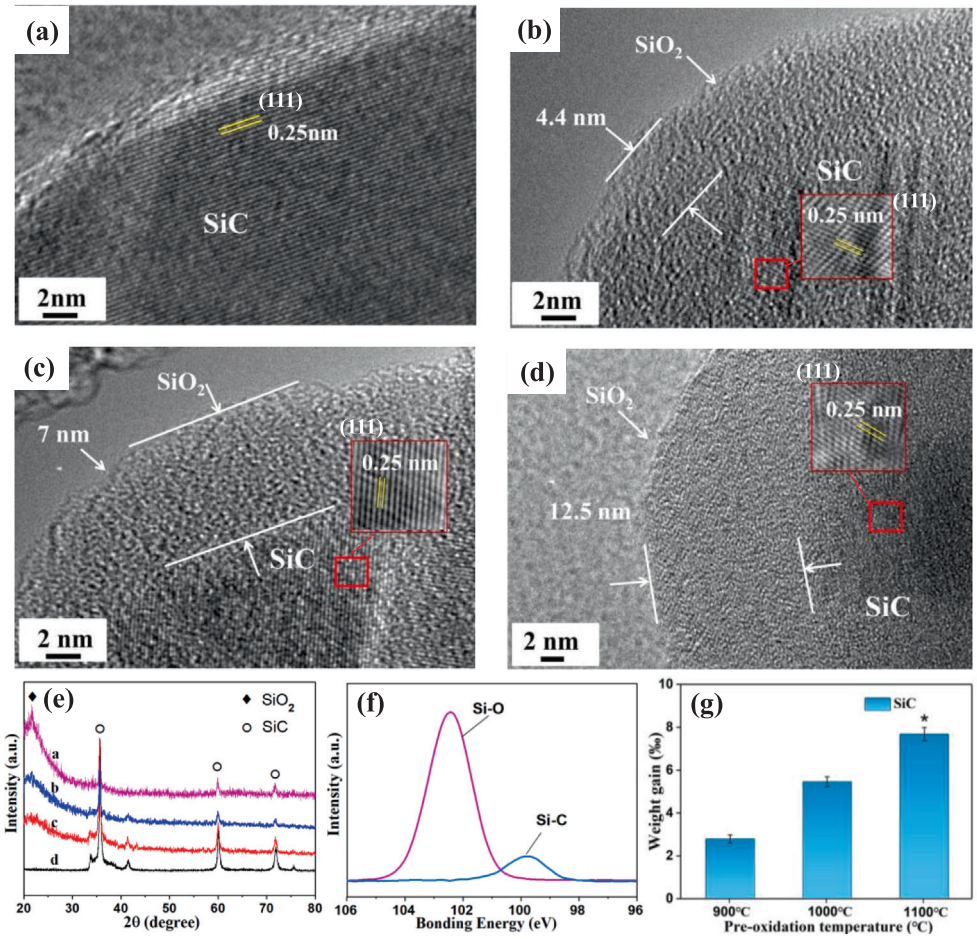

Fig. 3. HRTEM micrographs of (a) nano-SiC particles and pre-oxidized nano-SiC particles at (b) 900 °C, (c) 1000 °C, and (d) 1100 °C. (e) XRD results of nano-SiC particles and pre-oxidized nano-SiC particles. (f) XPS spectrum of Si 2p and (g) weight gain of the pre-oxidized nano-SiC particles ($P < 0.05$ (*)).

face area of sample: solution volume = 1 cm^2: 25 ml) [29]. After 7 weeks of immersion, these samples were removed from the SBF, cleaned with distilled water, dried in vacuum and weighted. Then the corrosion rates (mm/year) were calculated by weight loss according to ASTM-G31-72 standard [29].

Afterwards, the sample surface was cleaned with acid solution containing 0.2 g/ml CrO_3 to remove the degradation products. The surface morphologies of the samples before and after product removal were observed through SEM. Besides, pH values in SBF solutions were measured by a pH device (PHS-3C, Shanghai Lei Ci Device Works, China).

Biocompatibility

The biocompatibility assessment of the biocomposites was conducted by fluorescence staining, CCK-8 assay, and cell attachment using MG-63 cells. Dulbecco's modified Eagle medium (DMEM) with 10 vol% fetal bovine serum (FBS), 100 U/mL penicillin and 100 mg/mL streptomycin was prepared as medium. MG-63 cells were cultivated in aforesaid medium in a humidified incubator (37 °C, 5% CO_2). The samples were cleaned 3 times with phosphate buffer saline (PBS) solution, and then sterilized with ultraviolet light. Subsequently, the samples were respectively soaked in aforesaid medium (surface area of sample : medium volume = 1.25 cm^2: mL) for 24 h. The 50% and 100% extracts were collected and then put into 4 °C refrigerator for reserve.

For fluorescence staining, the MG-63 cells were cultivated in 24-well culture plates (5×10^3 cells/mL) with the 100% extracts for 3 days. Subsequently, the cells were digested and seeded upon glass slide, and then stained with Calcein-AM and Ethidium homodimer at 25 °C for 30 min. The stained cells were observed by a fluorescence microscope (BX60, Olympus, Japan). For CCK-8 assay, the MG-63 cells were cultured in 50% and 100% extracts for 1 day and 3 days, respectively. Afterwards, the cells were digested and seeded in 96-well plates with a density of 1×10^3 cell/ml. The cells, after incubation for 6 h, were cultivated with 10 μL CCK-8 for 2 h. Finally, the absorbance was measured at 450 nm by a plate reader (Paradigm Detection Platform, Beckman Coulter, USA). The cells incubated in the aforesaid medium without the extracts served as control.

In terms of cell attachment, the samples of ZS and ZS1000 biocomposites were sterilized by ultraviolet light for 2 h before placing in a 24-well plate. MG-63 cells were inoculated on the samples' surface with 4 ml DMEM and a concentration of 1×10^5 cell/ml. After 3 days, the samples were removed from the culture medium and washed with PBS. Next, the adherent MG-63 cells were fixed by 4% glutaraldehyde, dehydrated with ethanol and dried at 37 °C. Finally, the adherent MG-63 cells were observed with SEM.

Statistical analysis

Statistical analysis was conducted by SPSS13 software, and the results were represented by mean values ± standard deviations. Single factor variance analysis (ANOVA) was used for multi-group comparison with statistical significance of $P < 0.05$ (*).

Results and discussion

Pre-oxidized powders

The bright-field TEM micrographs of nano-SiC and pre-oxidized nano-SiC particles at 900 °C, 1000 °C, and 1100 °C were shown in Fig. 2. It can be seen that the nano-SiC particles presented regular spherical shape and distinct edges with uniform particle size distribution (Fig. 2a1). After pre-oxidation treatments, the edges of nano-SiC particles became blurred, and the particle size gradually increased with the pre-oxidation temperature (Fig. 2b1-d1). The electron diffraction ring was relatively clear in the selected area electron diffraction (SAED) pattern of nano-SiC particles, corresponding to the crystallization morphology (Fig. 2a2). In comparison, the SAED patterns of pre-oxidized nano-SiC particles (Fig. 2b2-d2) gradually became blurred as the diffraction spots faded away. Furthermore, the particle sizes of the nano-SiC particles with or without pre-oxidation treatments were measured in the bright-field TEM micrographs and calculated to obtain the statistical averages. Compared with the nano-SiC particles without pre-oxidation treatment (49.7 ± 2.4 nm) (Fig. 2a3), the average particle sizes of pre-oxidized nano-SiC particles at 900 °C, 1000 °C, and 1100 °C were 57.1 ± 2.2 nm, 62.9 ± 2.5 nm and 72.2 ± 3.1 nm, respectively (Fig. 2b3-d3).

The HRTEM micrographs of the particle edges were presented in Fig. 3a-d to further reveal the structural evolution of the particles after pre-oxidation treatments at different temperatures. It was clear that the nano-SiC particle showed lattice fringes with a spacing of 0.25 nm in accord with the (1 1 1) plane. After pre-oxidation, a continuous layer was uniformly formed on the surface of nano-SiC particles and the layer thickness increased with the pre-oxidation temperature. Moreover, the layer presented an amorphous structure as indicated by the fuzzy flocculent morphology. To reveal the composition of the newly formed layer, XRD analysis was carried out on the nano-SiC particles with and without pre-oxidation treatments (Fig. 3e). As can be seen, the patterns of pre-oxidized nano-SiC particles showed a new broadened diffraction peak at 20-–30°, in accord with the standard peak of amorphous SiO_2, compared with the pattern of nano-SiC particles. XPS analysis of the Si 2p spectrum (Fig. 3f) also presented two peaks at 102.2 eV and 100 eV, respective corresponding to Si—O bonding and Si—C bonding. Therefore, based on the XRD and XPS results, the formed layer on the surface of nano-SiC particles could be determined as amorphous SiO_2 layer. During the pre-oxidation treatments in air, reactions might occur on the surface of nano-SiC particles as follows [30,31]:

$$SiC + 2O_2 = SiO_2 + CO_2 \quad (1)$$

$$2SiC + 3O_2 = 2SiO_2 + 2CO \quad (2)$$

According to previous studies [32], the thickness of oxide layer could be calculated based on the weight gain of pre-oxidized nano-SiC particles. In the present study, the weight gain of the pre-oxidized nano-SiC particles at different temperatures were

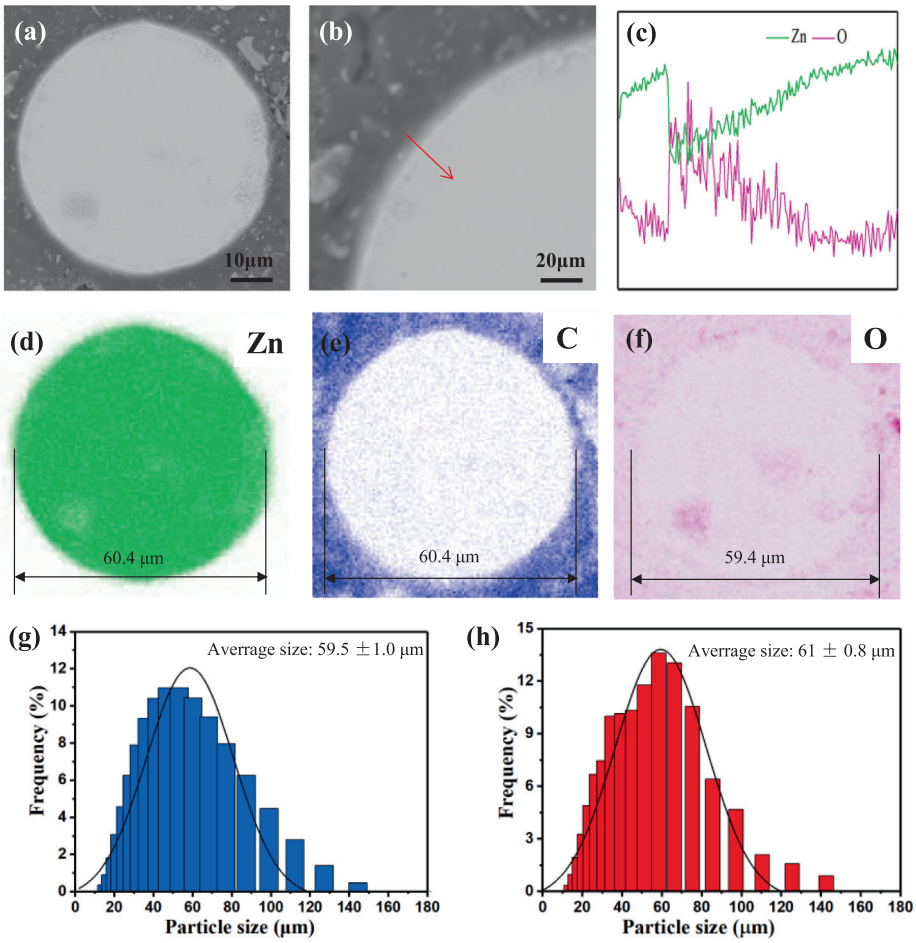

Fig. 4. (a, b) SEM micrographs of pre-oxidized Zn particle and corresponding (c) EDS line scannings and mappings of (d) Zn, (e) C, and (f) O elements. Particles size distribution of the (g) un-oxidized and (h) pre-oxidized Zn particles.

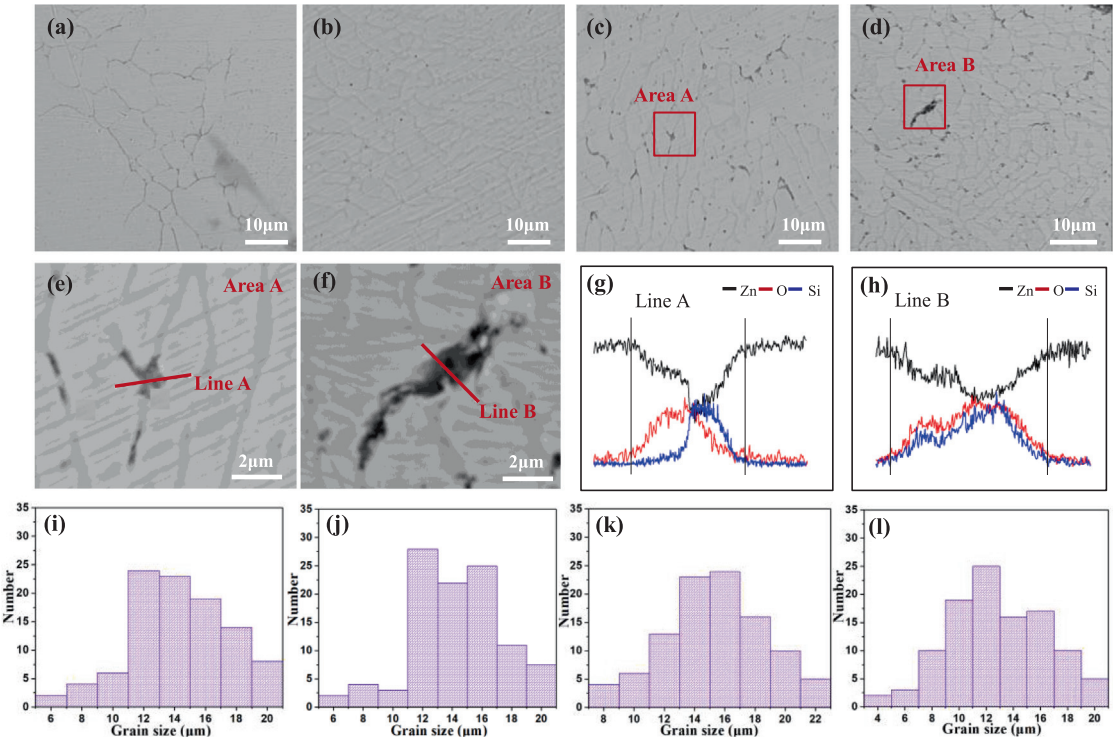

Fig. 5. SEM micrographs of the (a) ZS, (b) ZS900, (c) ZS1000 and (d) ZS1100 biocomposites. The high magnification SEM (HSEM) micrographs (e, f) corresponding to area A and area B in c and d, respectively. EDS line scanning on the (g) line A and (h) line B in the HSEM micrographs. The grain size distribution of the (i) ZS, (j) ZS900, (k) ZS1000 and (l) ZS1100 biocomposites.

recorded as shown in Fig. 3g. The calculated thickness of the oxide layer (SiO_2) on the surface of nano-SiC particles pre-oxidized at 900 °C, 1000 °C, and 1100 °C were approximately 3.5 nm, 7 nm and 10 nm, respectively. It was almost in line with the statistic thickness obtained from the TEM micrographs in Fig. 2a3-d3, further indicating the formation of SiO_2 layer on the surface of nano-SiC particles after pre-oxidation treatments.

The SEM micrographs of a representative pre-oxidized Zn particle were shown in Fig. 4a. It was clearly observed that the pre-oxidized Zn particle exhibited good sphericity and smooth edges. To evaluate the element composition, EDS line scanning and mapping were conducted on the boundary (Fig. 4b) and profile (Fig. 4a) of the pre-oxidized Zn particle, respectively. For the EDS line scanning (Fig. 4c), the increase of O element and decrease of Zn element across the particle edge illustrated the formation of surface oxide on the pre-oxidized Zn particle. As marked in the Fig. 4d-f, there existed a homogeneous overlapping region (~1 μm thickness) between the EDS mappings of O element and Zn element. Moreover, the average particle size increased from 59.5 ± 1.0 μm of the original Zn particles to 61 ± 0.8 μm of the pre-oxidized Zn particles (Fig. 4g and h). These results further indicated the formation of a continuous oxide layer on the surface of pre-oxidized Zn particles.

Microstructure of biocomposites

The microstructure of the biocomposites was observed by means of SEM and EDS, as illustrated in Fig. 5. Compared with ZS biocomposite, more uniform grain size distribution can be obtained in ZS900, ZS1000, and ZS1100 biocomposites (Fig. 5a-d). It is worth noting that some dark areas were visible at the grain boundaries of ZS 1000 and ZS1100 biocomposites, as displayed in Fig. 5c and d.

For better observation, high magnification SEM micrographs (Fig. 5e and f) and EDS line scanning (Fig. 5g and h) were further conducted at these dark areas. It is clear that the EDS scanning along line A in ZS1000 biocomposite and line B in ZS1100 biocomposite mainly included Zn, O and Si elements. In these dark areas, with the gradually reduced content of Zn element the content of Si element increased. And the content of O element maintained a consistent high level across the whole dark areas of lines A and B. Specifically, there was a co-existing area for Zn, Si and O elements on the line A and line B, revealing that the chemical composition of these dark areas might be in line with $x(ZnO)\cdot y(SiO_2)$. Moreover, it was notable that the co-existing length of Zn, Si and O elements in ZS1100 biocomposite (Fig. 5g) was longer than that of ZS1000 biocomposite (Fig. 5h), which may be associated with the thickness of interface products. The grain size distribution of the ZS, ZS900, ZS1000 and ZS1100 biocomposites was presented in Fig. 5i-l, where the average grain size of ZS, ZS900, ZS1000 and ZS1100 were 17.3 ± 2.5 μm, 14.7 ± 2.1 μm, 15.6 ± 2.7 μm and 13.8 ± 3.1 μm, respectively. No significant difference has been found in the grain size distribution of the biocomposites reinforced by nano-SiC particles with and without pre-oxidation treatments.

The composition of the biocomposites prepared via SLM was further verified by XRD patterns (Fig. 6a). It can be seen that the obvious characteristic peaks of Zn as the major phase in ZS, ZS900, ZS1000 and ZS1100 biocomposites. And no other phases were detected in ZS biocomposite. In contrast, the characteristic peaks of ZnO, SiO_2, and Zn_2SiO_4 could be seen in 2θ range of 20°~35° for ZS1000 and ZS1100 biocomposites (Fig. 6b), illustrating that the formation of interface products *via in situ* reaction during the SLM process. The *in situ* reaction occurred in the interface between the pre-oxidized nano-SiC and Zn matrix might be as follows [33]:

$$2ZnO + SiO_2 = Zn_2SiO_4 \quad (3)$$

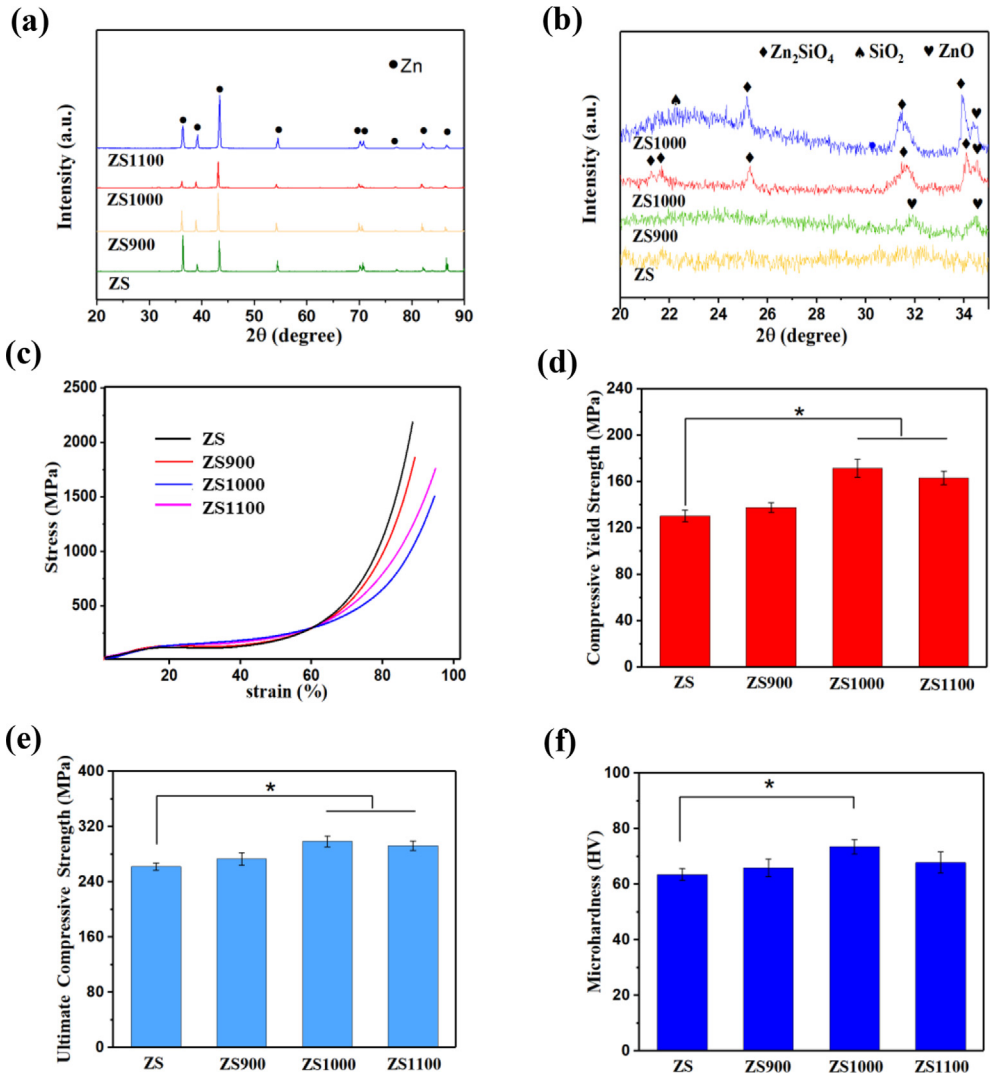

Fig. 6. (a) XRD patterns of the SLM-processed ZS, ZS900, ZS1000 and ZS1100 biocomposites with 2θ range of 20 ~ 90° and (b) magnified XRD patterns of the biocomposites with 2θ range of 20 ~ 35°. (c) The compressive stress–strain curves, (d) compressive yield strength, (e) ultimate compressive strength and (f) microhardness of the biocomposites.

Specifically, the XRD pattern of ZS900 biocomposite showed no characteristic peaks of Zn_2SiO_4, probably because too little SiO_2 was formed when nano-SiC particles were pre-oxidized at 900 °C and consequently the amount of interface products was beyond the detection limit of XRD technique. It was visible that obvious characteristic peaks of Zn_2SiO_4 appeared in the ZS1000 biocomposite, while both the characteristic peaks of SiO_2 and Zn_2SiO_4 presented in the ZS1100 biocomposite. The observation of powder microstructure showed that oxide layers were uniformly formed on the surface of nano-SiC particles and the layer thickness increased with the pre-oxidation temperature. And a much thicker SiO_2 layer formed on the surface of nano-SiC particles when pre-oxidized at 1100 °C. As a consequence, the amount of SiO_2 was too much to completely react with the ZnO on Zn particles, and the excess SiO_2 remained in the interface after *in situ* reaction between the pre-oxidized nano-SiC and Zn particles.

Mechanical properties

The mechanical properties of the biocomposites were measured by compression tests and microhardness tests. Representative compressive stress–strain curves for the ZS, ZS900, ZS1000 and ZS1100 biocomposites were shown in Fig. 6c. The compressive yield strengths increased to 137.6 ± 3.4 MPa for ZS900 biocomposite and 171.5 ± 5.1 MPa for ZS1000 biocomposite, followed by a slight decrease to 163.2 ± 3.3 MPa for ZS1100 biocomposite, compared with that of ZS biocomposite (130.3 ± 3.1 MPa) (Fig. 6d). It should be noticed that the compressive yield strength of the ZS1000 and ZS1100 biocomposites could better fit the mechanical properties of human cortical bone (170~190 MPa) than ZS biocomposite, especially in bone implant applications. Meanwhile, the ZS900, ZS1000 and ZS1100 biocomposites also exhibited higher ultimate compressive strength and microhardness than those of ZS biocomposite, as shown in Fig. 6e and f.

It is well known that the interface characteristics between the reinforcement and matrix play a crucial role in composites, especially for mechanical performance [34–37]. Many researches have demonstrated that by *in situ* interface reaction, a strong interface bonding could form between the matrix and reinforcement, which can improve the mechanical performance [34,38]. In the present study, no significant differences were found in grain sizes among the Zn/nano-SiC biocomposites with the incorporation of unoxidized and pre-oxidized nano-SiC particles. Therefore, the improvement of mechanical properties in the ZS1000 biocompos-

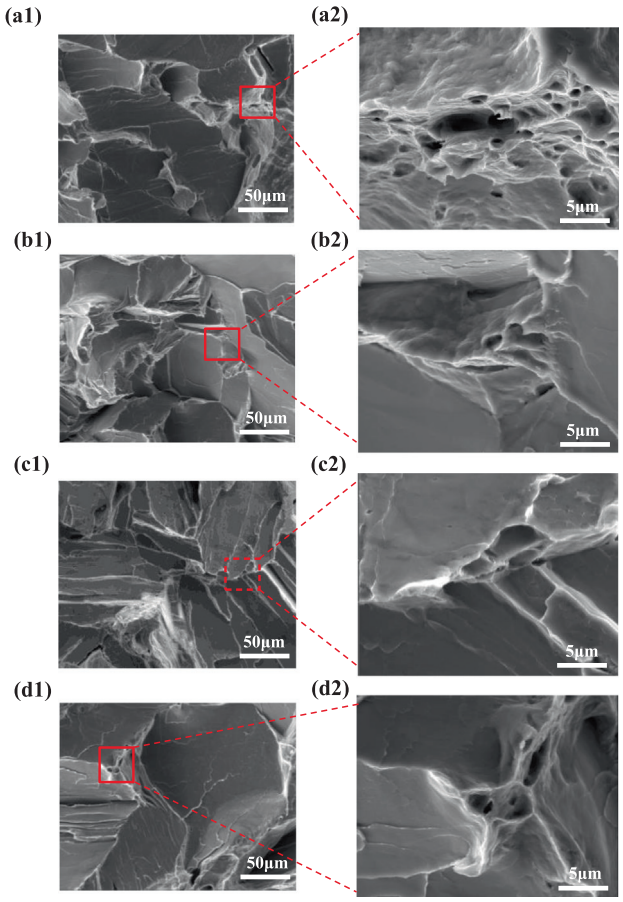

Fig. 7. The fracture surface morphology of the (a1) ZS, (b1) ZS900, (c1) ZS1000 and (d1) ZS1000 biocomposites, and the corresponding (a2-d2) HSEM micrograph.

ites could mainly be ascribed to the strengthening interface bonding between nano-SiC and Zn matrix by *in situ* interface reaction. Concretely, the interface product, formed by *in situ* reaction between the pre-oxidized nano-SiC and Zn matrix, served as an interface "bridge" to effectively transfer load from the Zn matrix to nano-SiC reinforcement, thereby improving the mechanical properties of the Zn/nano-SiC biocomposites. Moreover, it was notable that the compressive strength of ZS1100 decreased compared with ZS1000, which might be related to the excess remains of SiO_2 or the overmuch formation of Zn_2SiO_4 in the interface.

The representative fracture surface morphology of the ZS, ZS900, ZS1000 and ZS1100 biocomposites were displayed in Fig. 7. Apparently, the main fracture mode of all Zn/nano-SiC biocomposites was cleavage fracture, as characterized by cleavage cracks and steps (Fig. 7a1-d1) [39]. In general, cleavage fracture was viewed as brittle fracture. However, it can also be observed that some fine dimples, resulting from intergranular fracture, presented on partial fracture surface of the ZS and ZS900 biocomposites in the HSEM micrograph (Fig. 7a2 and b2). This revealed that the fracture mode of the Zn/nano-SiC biocomposites was a combination of both brittle and ductile fractures. In comparison with ZS and ZS900, a transformation tendency from intergranular fracture to transgranular fracture can be observed on the partial fracture surface of ZS1000 and ZS1100 biocomposites (Fig. 7c2 and d2). It has been reported that transgranular fracture is closely related to grain boundary strength and easily occurs as the grain boundary strength increases [40,41]. Thus, the transformation tendency from intergranular fracture to transgranular fracture in the present study might be related to the strong interface bonding formed by *in situ* reaction during SLM process, which makes it difficult for the Zn grains to be drawn out from the grain boundary.

Table 1
Electrochemical parameters calculated from polarization curves.

Composition	I_{corr} (μA/cm^2)	E_{corr} (V)	Corrosion rate (mm/year)
ZS	7.902 ± 0.344	−1.102 ± 0.012	0.150 ± 0.038
ZS900	8.342 ± 0.531	−1.214 ± 0.023	0.168 ± 0.065
ZS1000	9.710 ± 0.465	−1.270 ± 0.031	0.189 ± 0.041
ZS1100	6.394 ± 0.572	−1.173 ± 0.017	0.143 ± 0.027

Degradation properties

The electrochemical characteristics of the ZS, ZS900, ZS1000 and ZS1100 biocomposites were investigated by short-term polarization measurement. The potentiodynamic polarization curves were plotted in Fig. 8a, and the corresponding E_{corr}, I_{corr} and corrosion rates were calculated and listed in Table 1.

The corrosion rate of the biocomposites increased from 0.150 ± 0.038 mm/year of ZS biocomposite to 0.189 ± 0.041 mm/year of ZS1000 biocomposite, but no obvious differences in E_{corr} were observed among the Zn/nano-SiC biocomposites. The Nyquist plots in Fig. 8b presented a characteristically two semicircle-like curves corresponding to two time constants, which illustrated two capacitive loops for the EIS responses of the Zn/nano-SiC biocomposites. The high frequency capacitive loop was related to the oxide product film on the surface of biocomposites, while the low frequency capacitive loop was connected with the electron transfer and double layer effects in the interface of the biocomposites and electrolyte. The diameters of the semicircle-like curves of ZS900, ZS1000 and ZS 1100 biocomposites were smaller than that of ZS biocomposite, indicating a decreased corrosion resistance.

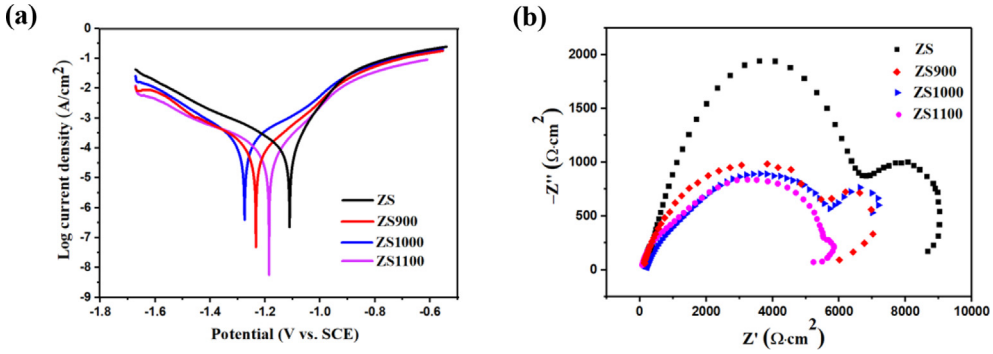

Fig. 8. (a) Polarization curves and (b) Nyquist plots of the SLM-processed ZS, ZS900, ZS1000 and ZS1000 biocomposites.

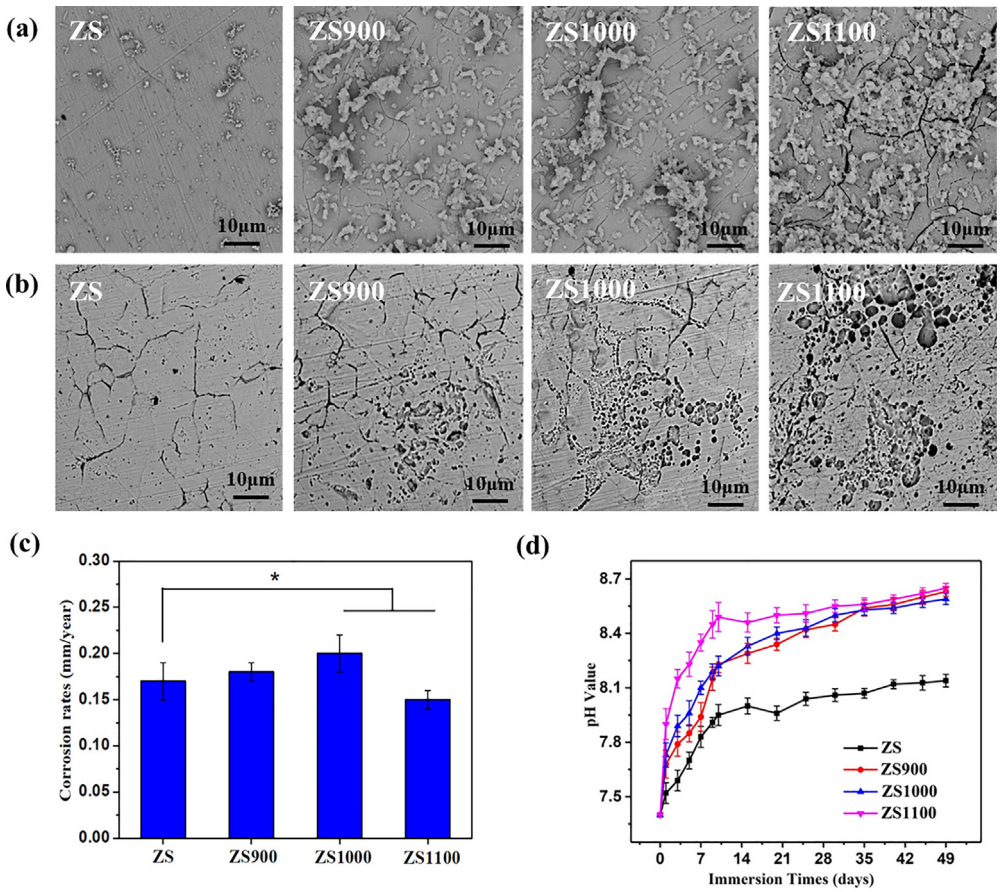

Fig. 9. Corrosion surface morphology of the biocomposites (a) before and (b) after the removal of corrosion products. (c) Corrosion rates calculated by weight loss. (d) pH variations with immersion time.

Immersion tests were used to evaluate the long-term degradation behavior of the Zn/nano-SiC biocomposites. After 7 weeks' immersion, the corrosion surface morphology of the ZS, ZS900, ZS1000 and ZS1100 biocomposites exhibited gradually increased corrosion precipitates with the increasing pre-oxidation temperature of nano-SiC particles, as illustrated in Fig. 9a. After removing the corrosion precipitates, the grain boundaries of Zn matrix were clearly visible, revealing a degradation process dominated by intercrystalline corrosion. In comparison, the surface of ZS900, ZS1000 and ZS1100 biocomposites showed more etch pits than ZS biocomposite (Fig. 9b), implying an intensified corrosion process.

Furthermore, the corrosion rates of the ZS, ZS900, ZS1000 and ZS1100 biocomposites were evaluated based on the weight loss after immersion for 7 weeks (Fig. 9c). Compared with ZS biocomposite (0.17 ± 0.02 mm/year), the corrosion rate increased to 0.18 ± 0.01 mm/year for ZS900 biocomposite and 0.20 ± 0.02 mm/year for ZS1000 biocomposite, respectively. The variation of pH values in SBF solution during the immersion was displayed in Fig. 9d. It was clear that the pH values increased rapidly at the initial stage of degradation and reached relatively stable state at the later period.

When immersed in SBF solution, Zn as an anode gradually released Zn^{2+} through oxygen reduction, resulting in a rapid increase in pH value at the initial stage of degradation due to the generation of OH^-. Subsequently, some corrosion products such as zinc phosphate gradually formed, making the pH alkaline and relatively steady at later period [42]. The degradation rates variations of Zn/nano-SiC biocomposites might involve interactions between the interface product, oxide layer and Zn matrix. On the one hand, the interface product Zn_2SiO_4 has high discharge capacity, which has been widely applied in the anode of lithium-ion batteries and electroluminescence materials [43]. Hence, the Zn_2SiO_4 distributed at the Zn/nano-SiC interface might be able to facilitate the electron transfer among Zn grains, thereby accelerating the degradation of the biocomposites. As a consequence, the degradation rate of ZS1000 biocomposite was higher than those of ZS and ZS900 biocomposites. On the other hand, it should be noticed that the corrosion rate of ZS1100 biocomposite (0.15 ± 0.01 mm/year) decreased compared with other biocomposites. Previous studies have reported that SiO_2 could promote the formation of calcium phosphate layer through hydrolysis reaction, and this protection layer could also hinder the penetration of corrosive solution [44]. Thus, this phenomenon might be related to the hydrolysis of excessive SiO_2, which led to more calcium phosphate precipitates on the sample surface and thereby slowed down the corrosion process.

Biocompatibility

Cytocompatibility of the ZS and ZS1000 biocomposites was evaluated by fluorescence staining, CCK-8 assay and cell attachment. The fluorescence morphologies of MG-63 cells after 3 days' cultivation in control group and the extracts of the ZS and ZS1000 biocomposites were illustrated as Fig. 10a, in which the live cells were stained green. It can be seen that both the ZS and ZS1000 biocomposites exhibited higher cell densities than that of control group, indicating a positive effect on cell proliferation, but no obvious differences can be observed between the ZS and

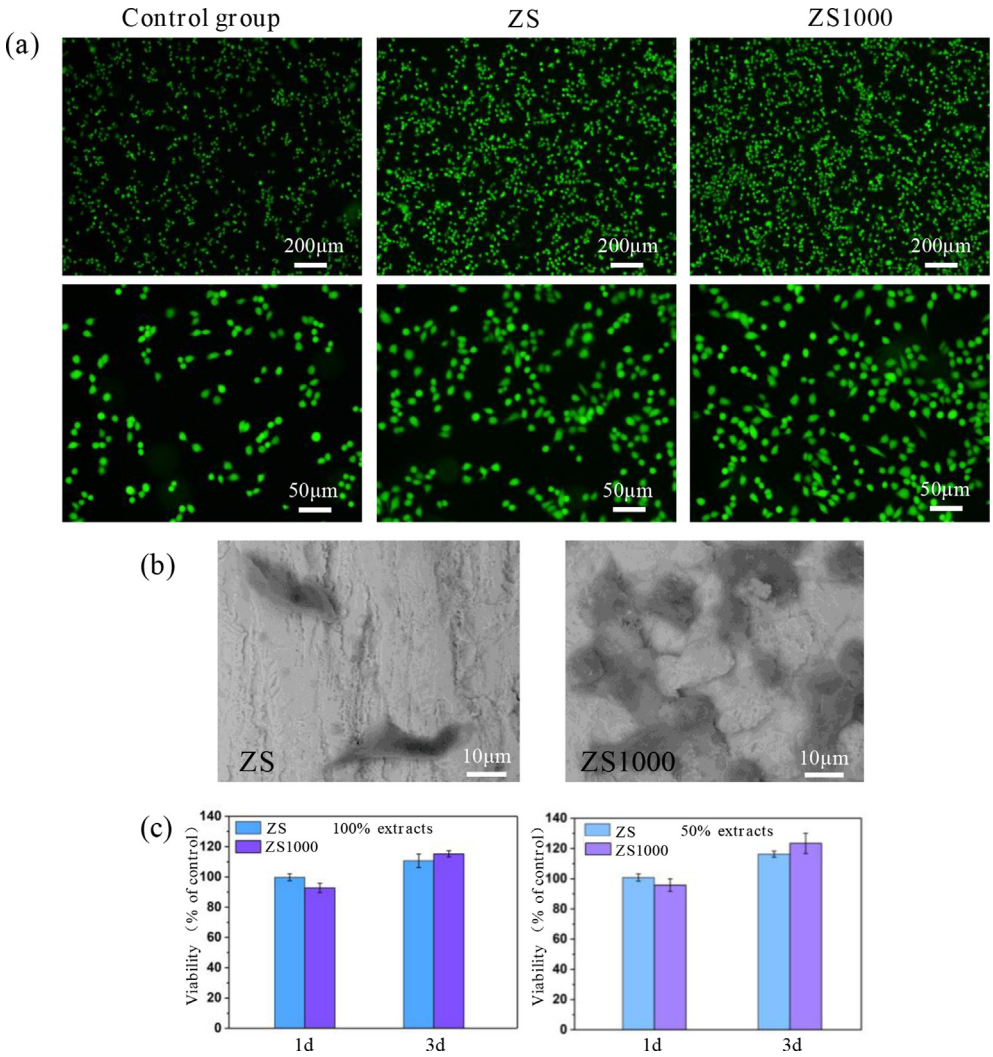

Fig. 10. (a) Fluorescence staining images of MG-63 cells after culturing in the extracts of the ZS and ZS1000 biocomposites for 3 days. (b) Adhesion morphology of MG-63 cells cultured on the ZS and ZS1000 biocomposites for 3 days. (c) CCK-8 assay results of MG-63 cells incubated for 1 day and 3 days in the 100% and 50% extracts of the biocomposites.

ZS1000 biocomposites. The representative cell adhesion morphology of MG-63 cells cultured on ZS and ZS1000 biocomposites for 3 days were displayed in Fig. 10b, where more cells were found attached to the surface of ZS1000 biocomposite compared with ZS biocomposite. Moreover, the cell viability was investigated by CCK-8 analysis after 1 day and 3 days' incubation in the 50% and 100% extracts (Fig. 10c), which maintained a value of more than 90%, illustrating good biocompatibility of the biocomposites based on ISO 19003-5 [45]. Besides, the results of CCK-8 analysis showed that cell viabilities of the ZS biocomposite had no significant differences compared with the ZS1000 biocomposite.

It has been reported that the cell proliferation is relevant to the ionic surroundings of the growth medium [46–48]. Therefore, the positive cell response might be ascribed to the release of Zn^{2+} and Si^{4+} from the biocomposites which could promote cell proliferation and differentiation [49–51]. Furthermore, both ZnO and SiO_2 have been widely studied as biomaterials owing to their good biocompatibility and attractive biological properties [52,53]. Additionally, it has been proven that the surface of SiO_2 possesses well hydrophilic groups, which is able to promote the adsorption of cell related proteins and thereby facilitates cell adhesion [54]. As a result, the *in situ* interface strengthened ZS1000 biocomposites prepared *via* SLS presented favorable biocompatibility to MG-63 cells, indicating potential applications for bone repair.

Conclusion

In this study, *in situ* interface reaction was innovatively introduced in Zn-SiC MMCs by a combined process of pre-oxidation and SLM, aiming to obtain Zn/nano-SiC biocomposites with strengthened interface bonding. A uniform oxide layer formed on the surface of nano-SiC (SiO_2) and Zn (ZnO) particles by pre-oxidation treatments, respectively. And the layer thickness increased with the pre-oxidation temperature. During the SLM process, *in situ* interface reaction was induced between the oxide layers of Zn (ZnO) and nano-SiC (SiO_2), resulting in the formation of interface product Zn_2SiO_4 in the biocomposite. Owing to the improved interfacial bonding, the compressive yield strength and ultimate compressive strength of ZS1000 biocomposite were improved by 31.6% and 13.5%, respectively, compared with ZS biocomposite. However, the excess SiO_2 or interface products pre-oxidized at 1100 °C weakened the interface strengthening effect. Compared with ZS biocomposite, the degradation rate of ZS1000 biocomposite slightly increased while that of ZS1100 biocomposite decreased. Meanwhile, cell culture tests proved well biocompatibility of the biocomposite in respect of cell activity, proliferation and adhesion. These findings indicated the practical applicability of this study in preparing Zn-based biocomposites with strong interface bonding for biodegradable implant fields.

Compliance with Ethics Requirements

This article does not contain any studies with human or animal subjects.

CRediT authorship contribution statement

Chengde Gao: Conceptualization, Methodology, Writing – review & editing. **Meng Yao:** Investigation, Writing–original draft. **Shuping Peng:** Visualization, Resources. **Wei Tan:** Investigation, Supervision. **Cijun Shuai:** Supervision, Funding acquisition.

Declaration of Competing Interest

The authors declare that they have no known competing financial interests or personal relationships that could have appeared to influence the work reported in this paper.

Acknowledges

This study was supported by the following funds: (1) Hunan Provincial Natural Science Foundation of China (2020JJ3047, 2019JJ50588); (2) The Natural Science Foundation of China (51935014, 82072084, 81871498); (3) The Provincial Key R & D Projects of Jiangxi (20201BBE51012); (4) JiangXi Provincial Natural Science Foundation of China (20192ACB20005); (5) National Engineering Research Center of Near-Net-Shape Forming for Metallic Materials Open Fund, SCUT (2020004); (6) Guangdong Province Higher Vocational Colleges & Schools Pearl River Scholar Funded Scheme (2018); (7) Innovation Team Project on University of Guangdong Province (2018GKCXTD001); (8) Technology Innovation Platform Project of Shenzhen Institute of Information Technology (PT2020E002).

References

[1] Mostaed E, Sikora-Jasinska M, Drelich JW, Vedani M. Zinc-based alloys for degradable vascular stent applications. Acta Biomater 2018;71:1–23.
[2] Zheng Y, Gu X, Witte F. Biodegradable metals. Mat Sci Eng R 2014;77:1–34.
[3] Tiffany AS, Gray DL, Woods TJ, Subedi K, Harley BAC. The inclusion of zinc into mineralized collagen scaffolds for craniofacial bone repair applications. Acta Biomater 2019;93:86–96.
[4] Jia Bo, Yang H, Han Yu, Zhang Z, Qu X, Zhuang Y, et al. In vitro and in vivo studies of Zn-Mn biodegradable metals designed for orthopedic applications. Acta Biomater 2020;108:358–72.
[5] Saranu R, Chanamala R, Rao Putti S. Processing, micro structures and mechanical properties of AZ91E, SiC and fly ash composites: A review. Mater Today Proc 2020;26:2629–35.
[6] El-Ghannam A, Greenier M, Johnson M, Marriott I. Synthesis and characterization of porous bioactive SiC tissue engineering scaffold. J Biomed Mater Res A 2020;108(11):2162–74.
[7] Wu L, Yuan Y, Hao F, Yang Z, Zhang J, Yu M. The effects of SiC foams on cell proliferation and differentiation in primary osteoblasts. J Hard Tissue Biol 2015;24(1):37–42.
[8] Rao T. An experimental investigation on mechanical and wear properties of Al7075/SiCp composites: effect of SiC content and particle size. J Tribol 2018;140(3):031601.
[9] Casalegno V, Salvo M, Ferraris M. Surface modification of carbon/carbon composites to improve their wettability by copper. Carbon 2012;50 (6):2296–306.
[10] Tong H, Qiu F, Zuo R, Shen P, Jiang Q. The Effect and Mechanism of Alloying Elements on Al/SiC Interfacial Reaction in Al Melt. Appl Surf Sci 2020;501:144265.
[11] Lü P, Wang X, Dong C, Peng C, Wang R. Preparation and characterization of different surface modified SiCp reinforced Al-matrix composites. J Cent South Univ 2020;27(9):2567–77.
[12] Yang W, Chen G, Qiao J, Zhang Q, Dong R, Wu G. Effect of Mg addition on the microstructure and mechanical properties of SiC nanowires reinforced 6061Al matrix composite. Mat Sci Eng A-Struct 2017;689:189–94.
[13] Panthglin C, Boontein S, Kajornchaiyakul J, Limmaneevichitr C. The Effects of Zr Addition on the Microstructure and Mechanical Properties of A356-SiC Composites. Int J Metalcast 2021;15(1):169–81.
[14] Park J, Lee J, Jo I, Cho S, Lee SK, Lee SB, et al. Surface modification effects of SiC tile on the wettability and interfacial bond strength of SiC tile/Al7075-SiCp hybrid composites. Surf Coat Tech 2016;307:399–406.
[15] Hashim J, Looney L, Hashmi MSJ. The wettability of SiC particles by molten aluminium alloy. J Mater Process Tech 2001;119(1-3):324–8.
[16] Gul A, Gürsoy Ö, Erzi E, Dispinar D, Kayali E. Aluminum Alloy with High Mg Content: Casting Studies for Microstructural Evolution, Phase Formation and Thermophysical Properties with Different Alloying Elements. In: Tiryakioğlu M, Griffiths W, Jolly M, editors. Shape Casting. The Minerals, Metals & Materials Series. Cham: Springer; 2019. p. 337–42.
[17] Guo R-F, Shen P, Li S-X, Shaga A, Jiang Q-C. High compressive strength in nacre-inspired Al-7Si-5Cu/Al_2O_3-ZrO_2 composites at room and elevated temperatures by regulating interfacial reaction. Ceram Int 2017;43 (9):7369–73.
[18] Yang Y, Lu C, Shen L, Zhao Z, Peng S, Shuai C. In-situ deposition of apatite layer to protect Mg-based composite fabricated via laser additive manufacturing. J Magnes Alloy 2021. doi: https://doi.org/10.1016/j.jma.2021.04.009.
[19] Yang Y, Cheng Y, Deng F, Shen L, Zhao Z, Peng S, et al. A bifunctional bone scaffold combines osteogenesis and antibacterial activity via in situ grown hydroxyapatite and silver nanoparticles. Bio-des Manuf 2021;4(3):452–68.
[20] Wang M, Zhao Yu, Wang L-D, Zhu Y-P, Wang X-J, Sheng J, et al. Achieving high strength and ductility in graphene/magnesium composite via an in-situ reaction wetting process. Carbon 2018;139:954–63.
[21] Li F, Wang W, Dang W, Zhao K, Tang Y. Wetting mechanism and bending property of Cu/Al_2O_3 laminated composites with pretreated CuO interlayer. Ceram Int 2020;46(11):17392–9.
[22] El-khair MTA, Lotfy A, Daoud A, El-Sheikh AM. Microstructure, thermal behavior and mechanical properties of squeeze cast SiC, ZrO_2 or C reinforced ZA27 composites. Mat Sci Eng A-Struct 2011;528(6):2353–62.
[23] Tripathi S, Bose R, Roy A, Nair S, Ravishankar N. Synthesis of hollow nanotubes of Zn_2SiO_4 or SiO_2: mechanistic understanding and uranium adsorption behavior. ACS Appl Mater Inter 2015;7(48):26430–6.
[24] Zhang H, Geng L, Guan L, Huang L. Effects of SiC particle pretreatment and stirring parameters on the microstructure and mechanical properties of SiCp/Al-6.8Mg composites fabricated by semi-solid stirring technique. Mat Sci Eng A-Struct 2010;528(1):513–8.
[25] Liu GW, Muolo ML, Valenza F, Passerone A. Survey on wetting of SiC by molten metals. Ceram Int 2010;36(4):1177–88.
[26] Hsia S-Y. Optimization of microextrusion preforming using taguchi method. Math Probl Eng 2013;2013:1–9.
[27] Guan K, Zhang L, Zhu F, Sheng H, Li H. Surface modification for carbon/carbon composites with Mg-CaP coating reinforced by SiC nanowire-carbon nanotube hybrid for biological application. Appl Surf Sci 2019;489:856–66.
[28] Tang Z, Huang H, Niu J, Zhang L, Zhang H, Pei J, et al. Design and characterizations of novel biodegradable Zn-Cu-Mg alloys for potential biodegradable implants. Mater Design 2017;117:84–94.
[29] Yang Y, Yang M, He C, Qi F, Wang D, Peng S, et al. Rare earth improves strength and creep resistance of additively manufactured Zn implants. Compos Part B-Eng 2021;216:108882.
[30] Shi Z, Ochiai S, Hojo M, Lee J, Gu M, Lee H, et al. The oxidation of SiC particles and its interfacial characteristics in Al-matrix composite. J Mater Sci 2001;36 (10):2441–9.
[31] Fu C, Yang Y, Huang Z, Liu G, Zhang H, Jiang F, et al. Investigation on the laser ablation of SiC ceramics using micro-Raman mapping technique. J Adv Ceram 2016;5(3):253–61.
[32] Ureña A, Martínez EE, Rodrigo P, Gil L. Oxidation treatments for SiC particles used as reinforcement in aluminium matrix composites. Compos Sci Technol 2004;64(12):1843–54.
[33] Isomäki I, Zhang R, Xia L, Hellsten N, Taskinen C. Thermodynamic assessment of ZnO-SiO_2 system. T Nonferr Metal Soc 2018;28(9):1869–77.
[34] Shuai C, He C, Peng S, Qi F, Wang G, Min A, et al. Mechanical Alloying of Immiscible Metallic Systems: Process, Microstructure, and Mechanism. Adv Eng Mater 2021;23(4):2001098.
[35] Shuai C, Peng B, Feng P, Yu L, Lai R, Min A. In situ synthesis of hydroxyapatite nanorods on graphene oxide nanosheets and their reinforcement in biopolymer scaffold. J Adv Res 2021. doi: https://doi.org/10.1016/j.jare.2021.03.009.
[36] Shuai C, Yuan X, Yang W, Peng S, Qian G, Zhao Z. Synthesis of a mace-like cellulose nanocrystal@Ag nanosystem via in-situ growth for antibacterial activities of poly-L-lactide scaffold. Carbohyd Polym 2021;262:117937.
[37] Qi F, Zeng Z, Yao J, Cai W, Zhao Z, Peng S, et al. Constructing core-shell structured $BaTiO_3$@carbon boosts piezoelectric activity and cell response of polymer scaffolds. Mat Sci Eng C-Mater 2021;126:112129.
[38] Dadbakhsh S, Mertens R, Hao L, Van Humbeeck J, Kruth J-P. Selective laser melting to manufacture "in situ" metal matrix composites: a review. Adv Eng Mater 2019;21(3):1801244.
[39] Pineau A, Benzerga AA, Pardoen T. Failure of metals I: Brittle and ductile fracture. Acta Mater 2016;107:424–83.
[40] Farahmand S, Monazzah AH, Soorgee MH. The fabrication of Al_2O_3-Al FGM by SPS under different sintering temperatures: microstructural evaluation and bending behavior. Ceram Int 2019;45(17):22775–82.
[41] Lin YC, Li L, He D-G, Chen M-S, Liu G-Q. Effects of pre-treatments on mechanical properties and fracture mechanism of a nickel-based superalloy. Mat Sci Eng A-Struct 2017;679:401–9.
[42] Yang H, Qu X, Lin W, Wang C, Zhu D, Dai K, et al. In vitro and in vivo studies on zinc-hydroxyapatite composites as novel biodegradable metal matrix composite for orthopedic applications. Acta Biomater 2018;71:200–14.
[43] Zhang S, Lu M, Li Y, Sun F, Yang J, Wang S. Synthesis and electrochemical properties of Zn_2SiO_4 nano/mesorods. Mater Lett 2013;100:89–92.

[44] Feng P, Kong Y, Liu M, Peng S, Shuai C. Dispersion strategies for low-dimensional nanomaterials and their application in biopolymer implants. Mater Today Nano 2021;15:100127.
[45] Watthanaphanit A, Rujiravanit R. Sericin-binded-deprotenized natural rubber film containing chitin whiskers as elasto-gel dressing. Int J Biol Macromol 2017;101:417–26.
[46] Qi F, Wang C, Peng S, Shuai C, Yang W, Zhao Z. A co-dispersed nanosystem of strontium-anchored reduced graphene oxide to enhance the bioactivity and mechanical property of polymer scaffolds. Mater Chem Front 2021;5(5):2373–86.
[47] Qian G, Zhang L, Wang G, Zhao Z, Peng S, Shuai C. 3D printed Zn-doped mesoporous silica-incorporated poly-L-lactic acid scaffolds for bone repair. Int J Bioprinting 2021;7(2):346.
[48] Gao C, Zeng Z, Peng S, Shuai C. Magnetostrictive alloys: Promising materials for biomedical applications. Bioact Mater 2022;8:177–95.
[49] Yang H, Qu X, Lin W, Chen D, Zhu D, Dai K, et al. Enhanced osseointegration of Zn-Mg composites by tuning the release of Zn ions with sacrificial Mg-rich anode design. ACS Biomater Sci Eng 2019;5(2):453–67.
[50] Han P, Wu C, Xiao Y. The effect of silicate ions on proliferation, osteogenic differentiation and cell signalling pathways (WNT and SHH) of bone marrow stromal cells. Biomater Sci 2013;1(4):379–92.
[51] Liu Y, Huang Na, Yu Y, Zheng C, Deng N, Liu J. Bioactive SiO_2@Ru nanoparticles for osteogenic differentiation of mesenchymal stem cells via activation of Akt signaling pathways. J Mater Chem B 2016;4(25):4389–401.
[52] Qi K, Cheng B, Yu J, Ho W. Review on the improvement of the photocatalytic and antibacterial activities of ZnO. J Alloy Compd 2017;727:792–820.
[53] Balamurugan A, Balossier G, Kannan S, Michel J, Rebelo AHS, Ferreira JMF. Development and in vitro characterization of sol-gel derived CaO-P_2O_5-SiO_2-ZnO bioglass. Acta Biomater 2007;3(2):255–62.
[54] Das I, De G, Hupa L, Vallittu PK. Porous SiO_2 nanofiber grafted novel bioactive glass-ceramic coating: A structural scaffold for uniform apatite precipitation and oriented cell proliferation on inert implant. Mat Sci Eng C-Mater 2016;62:206–14.